# NANOSCALE ENGINEERING OF BARIUM TITANATE USING COPPER (II) – TUNGSTEN (VI) DIPOLE PAIRS

by

Liam G. Saccucci-Bryan

A Thesis

Submitted to the Faculty of the

N.Y.S. College of Ceramics at Alfred University

In Partial Fulfillment of the Requirements

for the Degree of

Bachelor of Science in Biomaterials Engineering

Advisor: Dr. Steven C. Tidrow _____

Alfred, New York

May 2019

A Thesis Presented to

The Faculty of Alfred University

# NANOSCALE ENGINEERING OF BARIUM TITANATE USING COPPER (II) – TUNGSTEN (VI) DIPOLE PAIRS

by

Liam G. Saccucci-Bryan

In Partial Fulfillment of

The Requirements For

the Alfred University Honors Program

May 13, 2019

Under the Supervision of:

Chair: Dr. Steven C. Tidrow, Inamori Professor of Materials Science and Engineering

Committee Members:

Dr. Holly S. Shulman, Professor of Ceramic Engineering

Dr. Timothy J. Cox, Gertz Associate Clinical Professor of English

ACKNOWLEDGMENTS

My sincerest feelings of gratitude are unwaveringly extended to those instrumental in the completion of this thesis work and the degree in which it partially fulfills. I thank Dr. Steven C. Tidrow for the consistent and able guide as my thesis advisor and chair of the honors committee. Dr. Tidrow embodies the servant-leader mentality, as he is not shy to focusing his energies on the growth of others. I thank Ms. Genevieve Delfin for the constant support in ceramic processing and systematic monitoring of process variables. Her prowess and abilities as a ceramic engineer are unparalleled. I thank Mr. Alec Ladonis for his commitment to the diffraction efforts of this work. Mr. James Thiebaud and Dr. Darren Stohr contributed support in characterization efforts, and for that I am grateful. The Alfred University Grant for Undergraduate Students (ARGUS) and Kyocera Inc. financially supported research efforts, without which this work would not have been possible. Dr. Holly Shulman and Dr. Timothy Cox served faithfully as members of the honors committee. Finally, I would like to thank my friends and family for their support and encouragement throughout this process.

TABLE OF CONTENTS

PAGE

LIST OF TABLES

PAGE

LIST OF FIGURES

PAGE

## ABSTRACT

$BaTiO_3$ is a perovskite in which structural phase transitions are induced through polarization, and currently is one of the most widely used materials for ceramic capacitor technology. Above the $T_{C1}$ (Curie temperature one), $BaTiO_3$ exists as a single perovskite cubic structure. Based on theory stemming from the Clausius-Mossotti relation, polarization induced structural phase transitions can be engineered by increasing net energy conditions in the lattice. Past research has shown addition of discrete and localized electric fields have been shown to induce such phase transitions. Furthermore the substitution of permanent dipoles into $BaTiO_3$ have been shown to result in localized electric fields that are controllable and lend to enhanced electrical properties of materials possessing such compositions by Veerapandiyan[1]. To further investigate improvements in electrical properties by dipole substitution, compositions of $Ba(Cu^{2+},W^{6+})_xTi_{1-2x}O_3$, with x equal to 0, 0.00125, 0.0025, 0.005, 0.01, 0.025, 0.05, and 0.1 were prepared from solid oxide starting materials using solid-state synthesis reaction methodology. Room temperature X-ray Powder Diffraction and temperature dependent resistivity measurements have been conducted to characterize the synthesized materials. Experimental results demonstrate significantly greater electrical resistivity values when compared to undoped $BaTiO_3$ as well as $Ba(B'^{2+},B^{5+})Ti_{1-2x}O_3$ analog materials. As dipole substitution is increased, electrical resistivity systematically increases.

# INTRODUCTION

## A. ENERGY MATERIALS AND DEVICE REVIEW

Driven by population, capitalistic economy, and consciousness of environment, the demand for materials with energy conversion and storage applications is increasing steadily. Sourcing, disposal, renewal, and efficiency are at the forefront of optimization efforts among experts in the field. Among a myriad of energy storage devices, there are a few devices that are more commonplace, including batteries, fuel cells, and capacitors. Less common, but no less important, are devices like superconducting magnetic energy storage (SMES) and flywheels. To compare devices of this nature, power density and energy density of the respective devices or materials are often discussed. In order to establish a standardized method of comparing such materials, the Ragone plot, given in Figure 1, was created[2].

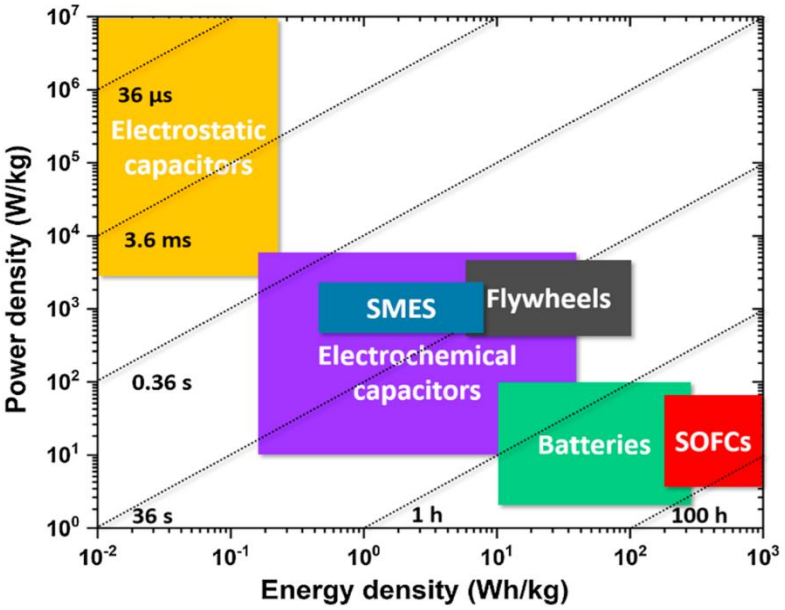


Figure 1 - The Ragone plot compares the power density and the energy density of various energy storage materials[2].

Although each class of device is used to store energy, the respective applications in which they are used differ because of the power density, energy density, and other material/device properties. The Ragone plot features several hashed lines crossing the charted area. These hashed lines are representative of characteristic charge/discharge time. Each device property that differs from the next are largely dependent on how the device stores energy. In capacitor materials and devices, a group of atoms are displaced from their original position in the lattice. Batteries and solid oxide fuel cells (SOFCs), on the other hand, store and convert energy through chemical reactions[2]. It is important to consider the varying classes of energy storage devices so that one may understand the importance of the electrostatic capacitors, also known as the dielectric capacitor, which from this point forward will simply be referred to as "capacitor".

1. Battery Technology

Battery technology has been the standard in many common commercial applications, and therefore is the most well-known to the general public when energy storage is discussed. The battery is often the energy storage device of choice for common applications such as remote controls, vehicle operations, and handheld electronics because battery technology was first conceived around 1600, and therefore is both well studied and reliable[3]. The technology at the core of the battery are electrochemical processes that work in the presence of an anode, cathode, and an electrolytic fluid. Within any single battery, there may be several cells configured in parallel. The bulk battery is designed in this

manner to maximize energy density and energy storage density. Figure 2 introduces the basic infrastructure of the modern battery[3].

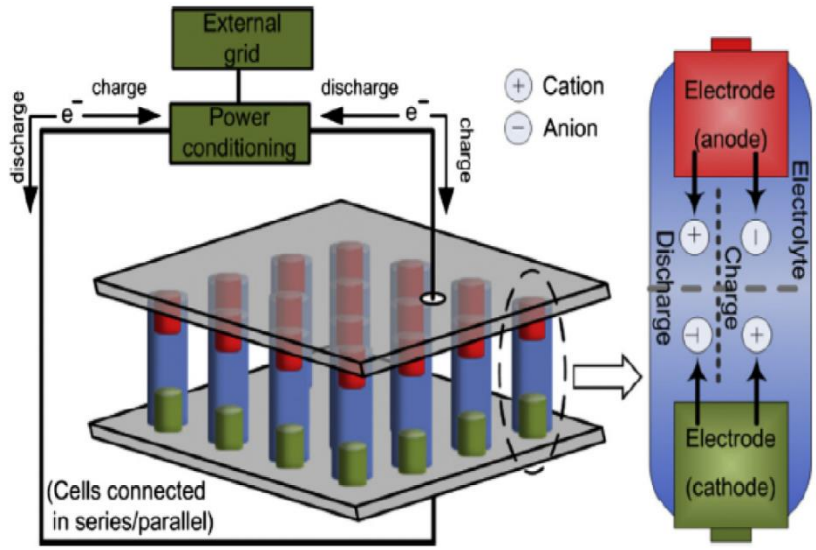


Figure 2 - Battery and electrochemical cell infrastructure. Charge differential created by separation of cation and anions cause flow of electrons[3].

There are various types of batteries, the details of which are beyond the scope of this literature review. It should be noted well, however, that each different class of battery has its own advantages and disadvantages. As such, a table is provided that briefly highlights a few important figures about the more common battery classes: lead-acid, NaS, NiCd, Li-ion, ZnBr, zero-energy breeder reactor assembly (ZEBRA), vanadium redox battery (VRB), and polysulfide bromide battery (PSB). The lead-acid battery is the oldest, and therefore the most well developed battery technology presented in Table I[3]. Environmental conditions are considered as well, with the most environmentally detrimental battery being the NiCd battery because of its use of heavy metals with acute toxicity.

Table I - Comparison of battery technologies[2].

| Technology | Advantages | Shortcoming |
|---|---|---|
| Lead-acid | Low cost, mature and readily available, reliable and easily replaced, suitable for power quality, UPS and spinning reserve applications. | High maintenance requirement, short cycling capability, low power and energy density, Slow charge, Low weight-to-energy ratio, thermal management requirement, and has an environmental hazard (i.e., toxic component). |
| NaS | Relatively high power and energy density, efficient, economical for power quality and peak shaving purposes. | Heat source requirement, high cost. |
| NiCd | Relatively high energy density, relatively low cycling capability, high mechanical resistance, low maintenance requirement, suitable for power tools, emergency lighting, generator starting, telecoms and portable devices. | High cost, environmental hazard (e.g., toxic heavy metal "cadmium"), memory effect in which case the charge on the battery becomes full after a couple of full discharges. |
| Li-ion | Relatively high power and density, almost 100% efficient, higher cycling capacity, fast response to charge and discharge operations. | High cost, degrades at high temperatures. |
| ZEBRA | Ability to withstand limited overcharge and discharge with better safety features and a relatively high electrochemical cell voltage (2.58 V), suitable for load-leveling applications in the industry. | Lower power and energy density compared to NaS, suitable for large capacity applications (>20 kWh capacity), only one manufacturer produces this battery technology (i.e., Beta R&D in the UK). |
| VRB | High round-trip efficiency (RTE), suitable for improved power quality, UPS, peak-shaving, integration of renewable resources. | |
| PSB | Operates at room temperature. | Relatively low DC output voltage (about 1.5 V). |
| ZnBr | | Lower RTE and lifespan compared to the conventional lead-acid, suffers material corrosion and dendrite formation. |
| Redox Flow batteries | Relatively high power and energy density, useful for large-scale applications. | High cost, complex standardization. |

2. Solid Oxide Fuel Cells

Solid oxide fuel cells (SOFCs) are another common class of energy storage device. In fact, the concept of SOFCs technology and battery technology is by and large the same. There are two key differences between battery technology and SOFC technology. The first difference is that SOFCs contain a solid electrolyte for charge carrier transport. Secondly, there is a portion of the SOFC that contains fuel, and another that contains an oxidizing agent. Oxygen ions are used as charge carriers, and are reduced at the cathode, or oxidized at the anode. On the oxidizing agent side of the fuel cell, the oxygen is active with electrons present in the material and form oxygen ions that migrate as charge carriers through the solid electrolytic substance[4]. Figure 3[4] demonstrates a common construction of an SOFC.

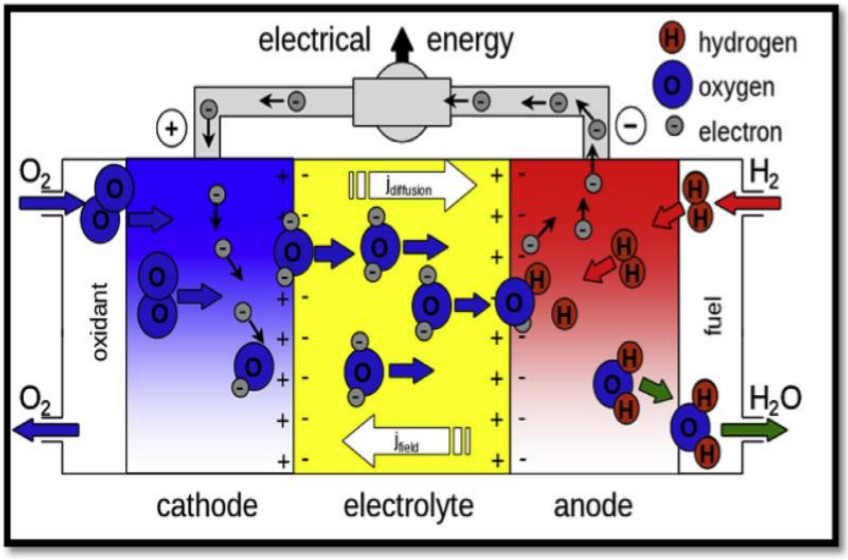


Figure 3 – Commonplace architecture of the SOFC. SOFCs work by directly oxidizing a fuel to create charge carrier motion and therefore electric current[4].

The key advantages of SOFCs are their durability, high efficiency ratings, and the less strict list of materials that can be used for energy generation. Often, the materials used in SOFCs can be less toxic than those used in batteries[4]. However, according to the Ragone plot, both batteries and SOFCs show low power density as well as a charge/discharge time on the order of hours to multiple hundreds of hours, and even thousands of hours.

Dielectric capacitors demonstrate properties that are the opposite: high power density with rapid charge/discharge times. One of the primary appeals of dielectric capacitors (capacitors) are their incredibly fast charging and discharging times regardless of the class of capacitor that is being investigated. Basically, when investigating the engineering of capacitors, it boils down to a materials science and engineering research and development problem in which stakeholders must understand with full aptitude what

the desired performance characteristics of the capacitors are. Questions as to whether the target device requires a high dielectric permittivity, a high breakdown strength, both, or neither, must be discussed by the development team. Dielectric permittivity is defined by Fuley and Lee as "a parameter that expresses the ability of a material to store charge, expressed as $\varepsilon = \sigma_s/E$, where $\sigma_s$ is the surface charge density and E is the electric field." Breakdown strength is roughly defined by the same scholars as a phenomenon that causes permanent materials damage and altering of properties, often in an undesirable fashion[5]. Two primary capacitor classes exist, categorized by the type of material that they are created with. Dielectric ceramics and polymer-based materials are commonly used in commercial capacitors, but each in different categories. Dielectric ceramics are known to demonstrate low breakdown strength values along with high permittivity values. Polymer based materials often display opposite properties, with high breakdown strength and low permittivity. A chart demonstrating the relationship of breakdown strength with permittivity is given below in Figure 4[2]. From Figure 4, the trend between breakdown strength and permittivity is inversely proportional.

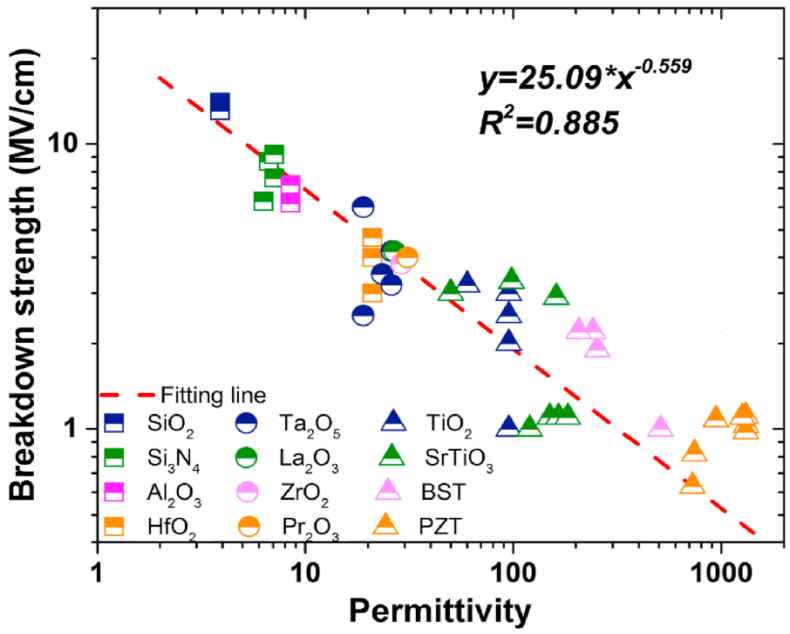


Figure 4 - Inversely proportional trend is illustrated between breakdown strength and permittivity of materials[2].

Since the energy density of capacitors scales as a linear function of permittivity and the square of the breakdown strength, engineering efforts are being prompted to develop dielectric materials with high permittivity values coupled to high breakdown strength values. Due to the difference in materials and properties displayed within the different classes of capacitors, the synthetic methods and routes differ in distinct ways[2].

## 3. Dielectric Ceramic Synthesis

A variety of synthesis methods are used to form dielectric ceramics. A common dielectric ceramic is barium titanate, chemical formula $BaTiO_3$, in which the synthetic

methods can be mapped to most dielectric ceramics. All methods require proper mixing of the starting materials so that uniform phases are formed throughout the synthetic pathways. Figure 5[6] gives the variety of common synthesis methods for barium titanate and many other dielectric ceramics[6].

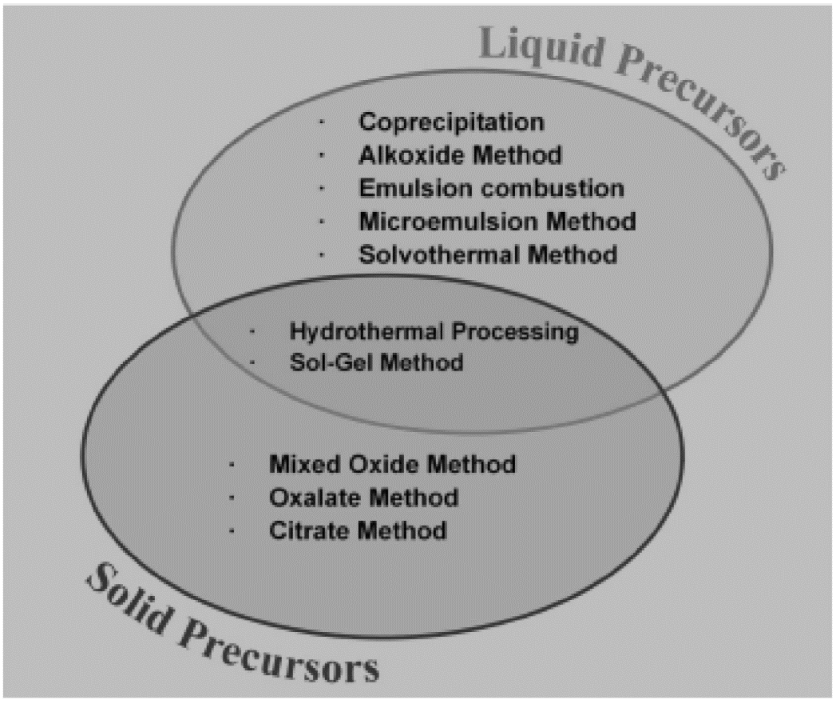


Figure 5 - Overview of synthesis methods for fabrication of ceramic dielectric materials[6].

The original, and typically the easiest method for processing barium titanate is the mixed oxide method. Starting from barium carbonate and titanium dioxide, the mixed oxide method is contingent on the diffusion of barium ions into the titanium dioxide lattice. Unfortunately, this method typically leads to non-uniform mixing of particles, less phase pure sintered materials, and non-uniform ion distribution within the lattice if careful

processing considerations are not adhered to. These undesired traits lead to dielectric ceramic materials that underperform when compared to their sol-gel synthesized analogs. Therefore, sol-gel and other liquid based synthesis routes have recently been used more often when high electrically performing dielectric ceramics are desired. [6]

## B. BARIUM TITANATE

Barium Titanate, chemical formula $BaTiO_3$, belongs to the class of materials named perovskites. A high temperatures greater than about 130 °C, $BaTiO_3$ forms the "ideal" Pm3m perovskite structure that upon cooling to room temperature is slightly extended in the direction of the c-axis thus causing it to be classified as a tetragonal structure possessing ferroelectric properties[7]. $BaTiO_3$ has lattice parameters reported to be a = b = 3.98 Å, c = 4.03 Å, and $\alpha = \beta = \gamma = 90°$ at room temperature (298 K)[8]. The unit cell of $BaTiO_3$ is shown in Figure 6.

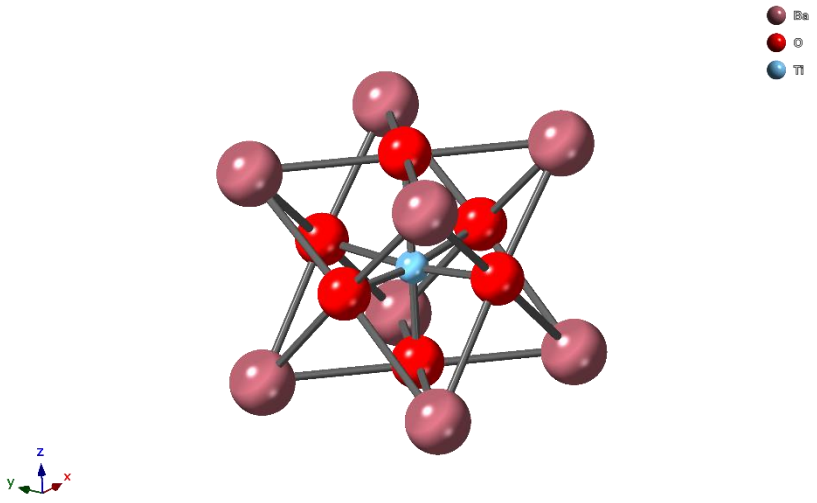


Figure 6 - The unit cell structure of $BaTiO_3$: a = b = 3.98 Å, c = 4.03 Å, and $\alpha = \beta = \gamma = 90°$ at room temperature [2].

Historically, $BaTiO_3$ has been the material of choice for ceramic capacitor technologies because it demonstrates several desirable qualities including high relative permittivity values [7,9,10]. Capacitance is charge stored in the electrical disparity between positive and negative charges as the result of a polarization event. The energy storage density of $BaTiO_3$ materials has recently been increased by up to two full orders of magnitude using Ga – Ta dipole pairs to form the solid solution $Ba(Ga,Ta)_xTi_{1-2x}O_3$[1]. One order of magnitude in breakdown strength translates into two orders of magnitude in energy storage density for the same relative permittivity[11]. These previous efforts motivate the work of this thesis which focuses on the dipole pair Cu – W through the formation of the solid solution $Ba(Cu,W)_xTi_{1-2x}O_3$.

# MATERIALS AND METHODS

## A. BATCHING

$Ba(Cu,W)_xTi_{1-2x}O_3$, with x = 0.00, 0.00125, 0.0025, 0.005, 0.01, 0.025, 0.05, 0.1, was prepared in stochiometric batches of 70 g each. $BaCO_3$, $TiO_2$, $WO_3$, and CuO were massed into 200 mL Nalgene high density polyethylene (HDPE) jars in the appropriate stochiometric ratios. 200 g of 6 mm Yttria-stabilized-zirconia (YSZ) were added to the jars along with 100 mL of 2-propanol and milled for 20 hours to ensure particle sizes of $d_{50}$ < 0.7 µm and a sufficiently homogenous slurry. The details regarding each chemical used in the fabrication of materials is found in Table II. Finally, each batch was dried in a Pyrex tray at 150 °C for 24 hours. To discourage hydration, the dried powders were stored in desiccant chambers until the calcination procedure was performed.

Table II - Details on reagents used in material fabrication.

| Chemical Name | Purity | Particle Mesh | Supplier |
|---|---|---|---|
| **$BaCO_3$** | 99.997% | -22 | Alfa Aesar™ |
| **$TiO_2$** | 99.995% | -22 | Alfa Aesar™ |
| **$WO_3$** | 99.998% | -325 | Alfa Aesar™ |
| **CuO** | 99.995% | -325 | Alfa Aesar™ |
| **2-Propanol** | ≥99.9% | N/A | Fisher Chemical™ |

B. CALCINING

Two pellets per composition were uniaxially pressed to 2000 metric ton in a 30 mm hardened stainless-steel die. Each pellet was placed on a platinum foil and fired at 1250 °C for 10 hours. The samples were heated and cooled uniformly at a rate of 5 °C per minute in an air atmosphere using a box furnace (KSL-1700X MTI Corporation). Following calcination, the powders were attrition milled in 2-propanol for five minutes and subsequently dried in Pyrex pans at 150 °C for 24 hours. Room temperature X-ray powder diffraction was performed on the dried powders to monitor the phase composition of the materials, and the density of each pellet was measured and recorded directly before and after calcination.

C. SINTERING

Without the use of sintering aids or binders, the dried powders were uniaxially pressed to 2000 metric ton in a 30mm hardened stainless-steel die. The pellets were then sealed sequentially within two vacuum bags and cold isostatically pressed at 170 MPa for 30 minutes. The pellets were placed on platinum foil and sintered at 1350 °C under air atmosphere for 24 hours. The box furnace was uniformly heated and cooled at 1.84 °C per minute. Room temperature X-ray powder diffraction was performed on the dried powders to monitor the phase composition of the materials, and the density of each pellet was measured and recorded directly before and after sintering.

D. WAFERING

Each pellet was cold mounted in epoxy and left to set at room temperature for 24 hours. A CNC controlled diamond bladed wafering saw was used to create 0.8 mm thick wafers from each pellet. The ring of epoxy was removed, and the wafer was placed in a drying oven at 150 °C for 3 hours to evaporate any residual water that was introducing during the wafering process. To form an electroded wafer, gold metal was sputter for 60 seconds to approximately 500 nm on each side.

## CHARACTERIZATION INSTRUMENTATION

### A. ROOM TEMPERATURE X-RAY DIFFRACTION

X-ray powder diffraction (XRD) was used to characterize phases through the material fabrication process. XRD was performed on calcined powders and sintered wafers for each sample composition. Each diffraction pattern was taken at room temperature using a Bruker D8 Advanced diffractometer. Each scan was taken between 20° and 100° 2θ.

### B. RESISTIVITY MEASUREMENTS

Resistivity measurements were taken with an instrument complex consisting of a Qex Centurion furnace, a Keithley 6487 picoammeter, and LabVIEW software (Z-DAQ V.1-12) controlling the Keithley 6487 as the voltage source. The measurement setup as adopted from Veerapandiyan et al. Figure 7 [1] shows a schematic of the instrumental set-up.

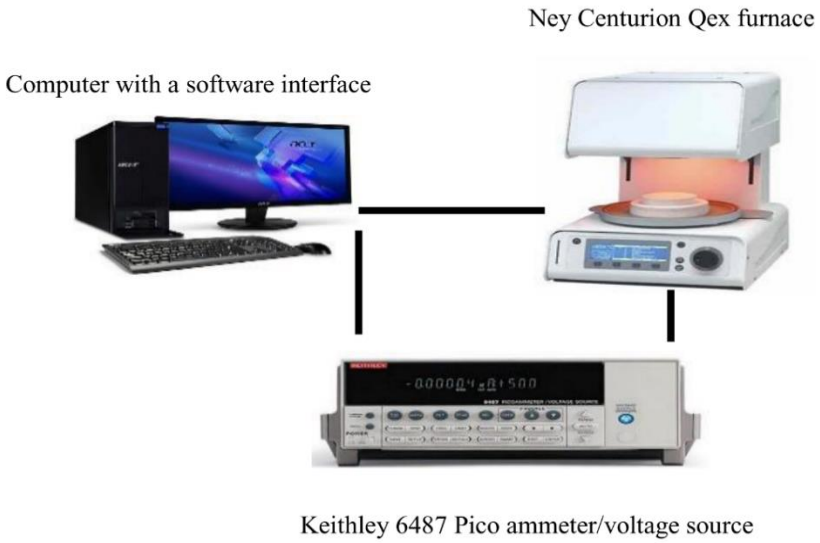


Figure 7 – Resistivity measurement instrumentation set-up. The system can be used for temperature dependent resistivity measurements from 297 K to 1297 K[1].

## RESULTS AND DISCUSSION

### A. THEORETICAL DENSITY

Barium Titanate was substituted in the B-site for $Ti^{4+}$ with discrete dipoles, using $Cu^{2+}$ and $W^{6+}$, forming $Ba(Cu,W)_xTi_{1-2x}O_3$. For the ease of discussion, Table III details how each sample composition will be referred to.

Table III – Sample name and composition details.

| **Sample Name** | **$Ba(Cu,W)_xTi_{1-2x}O_3$** |
|---|---|
| BT001 | X = 0.0 |
| BT002 | X = 0.00125 |
| BT003 | X = 0.0025 |
| BT004 | X = 0.005 |
| BT005 | X = 0.01 |
| BT006 | X = 0.025 |
| BT007 | X = 0.05 |
| BT008 | X = 0.1 |

Literature values for barium titanate density are cited to be between 6.02 $\frac{g}{cm^3}$ and 6.08 $\frac{g}{cm^3}$ [12-15], and the value chosen to compare to is the average of the two cited values, 6.05 $\frac{g}{cm^3}$ . The theoretical density has been calculated for BT001, BT002, BT003, BT004, BT005, BT006, BT007, and BT008 at the following points during fabrication: directly prior to calcination, directly prior to cold-isostatic pressing, directly prior to sintering, and directly after sintering and cooling. Tables IV – VII give calculated and theoretical density values for each sample at each respective step.

Table IV – Density and theoretical density values taken directly prior to calcination.

| **Sample Name** | **Density [$\frac{g}{cm^3}$]** | **Theoretical Density [%]** |
|---|---|---|
| BT001 | 2.59 ± 0.01 | 42.89 |
| BT002 | 2.63 ± 0.08 | 43.50 |
| BT003 | 2.49 ± 0.14 | 41.21 |
| BT004 | 2.63 ± 0.08 | 43.54 |
| BT005 | 2.85 ± 0.11 | 47.19 |
| BT006 | 2.94 ± 0.12 | 48.58 |
| BT007 | 2.94 ± 0.13 | 48.62 |
| BT008 | 3.06 ± 0.12 | 50.59 |

Two pellets of each composition were pressed for calcination, therefore the density and theoretical density values reported in Table IV are calculated mean values. The maximum sample standard deviation is ±0.14 $\frac{g}{cm^3}$, indicating that the density is uniform from pellet to pellet within the sample composition.

Table V – Density and theoretical density values taken directly prior to cold isostatic pressing.

| **Sample Name** | **Density [$\frac{g}{cm^3}$]** | **Theoretical Density [%]** |
|---|---|---|
| BT001 | 3.60 | 59.57 |
| BT002 | 3.64 | 60.15 |
| BT003 | 3.57 | 58.96 |
| BT004 | 3.54 | 58.61 |
| BT005 | 3.74 | 61.83 |
| BT006 | 3.91 | 64.82 |
| BT007 | 4.00 | 66.06 |
| BT008 | 4.10 | 67.80 |

After calcination, the theoretical density values for all samples are shown to increase compared to pre-calcination theoretical density values on average 16.46 ± 1.10 %.

Table VI – Density and theoretical density values taken directly prior to sintering.

| **Sample Name** | **Density [$\frac{g}{cm^3}$]** | **Theoretical Density [%]** |
|---|---|---|
| BT001 | 3.82 | 63.13 |
| BT002 | 3.80 | 62.74 |
| BT003 | 3.77 | 62.39 |
| BT004 | 3.81 | 62.97 |
| BT005 | 3.96 | 65.44 |
| BT006 | 4.37 | 72.17 |
| BT007 | 4.22 | 69.73 |
| BT008 | 4.35 | 71.94 |

After cold isostatic pressing at 170 MPa for 30 mins, the theoretical density values increased 4.09 ± 1.42 %.

Table VII – Density and theoretical density values taken directly post sintering and cooling.

| **Sample Name** | **Density [$\frac{g}{cm^3}$]** | **Theoretical Density [%]** |
|---|---|---|
| BT001 | 5.96 | 98.55 |
| BT002 | 5.24 | 86.54 |
| BT003 | 4.67 | 77.13 |
| BT004 | 4.55 | 75.27 |
| BT005 | 4.01 | 66.23 |
| BT006 | 4.08 | 67.47 |
| BT007 | 4.05 | 66.96 |
| BT008 | 4.15 | 68.54 |

Finally, after sintering and cooling, the samples increased in theoretical density by 9.52 ± 14.67 %. The increase in theoretical density values caused by sintering has a standard deviation of 14.67% and is very high compared to other steps. The high standard deviation value results due to each sample varying greatly in the amount that it increased in density, and some samples (BT006, BT007, and BT008) decreased in density. Table VIII summarizes the increase in theoretical density values at each step.

Table VII – Theoretical density change per primary processing step.

| Sample Name | Theoretical Density Change Pre-Cold Isostatic Pressing [%] | Theoretical Density Change Pre-Sintering [%] | Theoretical Density Change Post-Sintering [%] |
|---|---|---|---|
| BT001 | 16.68 | 3.56 | 35.42 |
| BT002 | 16.65 | 2.59 | 23.80 |
| BT003 | 17.75 | 3.43 | 14.74 |
| BT004 | 15.08 | 4.36 | 12.29 |
| BT005 | 14.64 | 3.61 | 0.79 |
| BT006 | 16.24 | 7.35 | -4.71 |
| BT007 | 17.44 | 3.66 | -2.76 |
| BT008 | 17.22 | 4.13 | -3.40 |

From plotting the theoretical density change post-sintering, there is an inverse proportional relation to the amount of dipole substituted into the lattice and the increase in theoretical density increase. Figure 8 demonstrates the correlation between dipole substitution and theoretical density change before and after sintering.

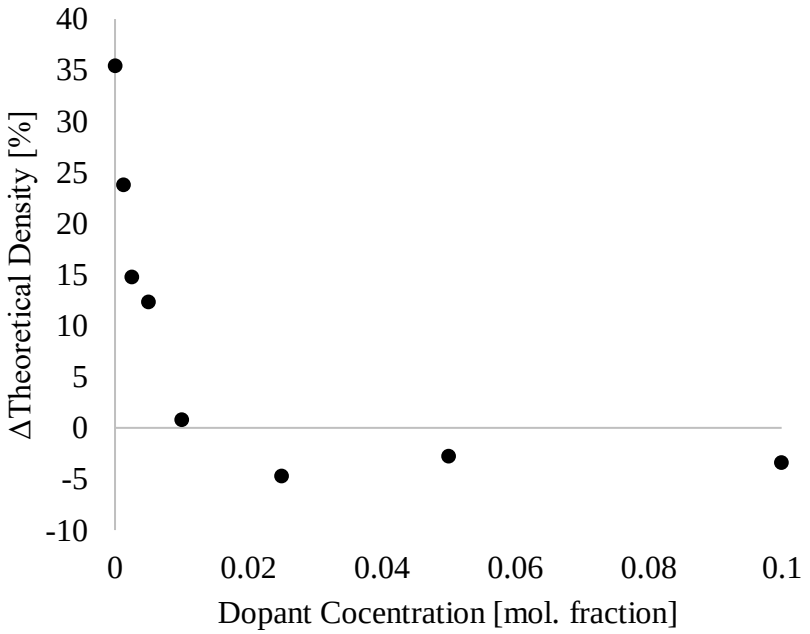


Figure 8 – Change in theoretical density as a function of dopant concentration (post-sintering compared to pre-sintering).

The densification restriction that is observed as a function of dopant concentration may correspond to the crossover region, described by Veerapandiyan, during which higher resistivity materials occur because of dipole strength overcoming the strength of the matrix field[1]. According to Fulay, et al.[5] polarization of atoms occurs when an electric field is applied, including perhaps an internal constructed dipole field. In order to pursue higher density sintered ceramics, a sintering temperature profile that soaks at a higher temperature and for a longer time should be considered.

B. ROOM TEMPERATURE X-RAY DIFFRACTION

Room temperature X-ray diffraction (RTXRD) was conducted on samples BT, BT001, BT002, BT003, BT004, BT005, BT006, BT007, and BT008 after calcination and after sintering to systematically monitor perovskite phase formation progress. Figure 8 – Figure 15 give the RTXRD patterns for each sample. All sample patterns were taken using the same instrumentation, detailed in the "CHARACTERIZATION INSTRUMENTATION" section. In Figure 9 – Figure 16, the powder diffraction file generated from the International Centre for Diffraction Data Database (ICDD) PDF-4+ software for both Barium Titanate (00-005-0626 $BaTiO_3$) and Barium Orthotitanate (00-035-0843 $Ba_2TiO_4$) is plotted. These diffraction patterns are provided because they are the two primary phases that appear in the fabricated materials.

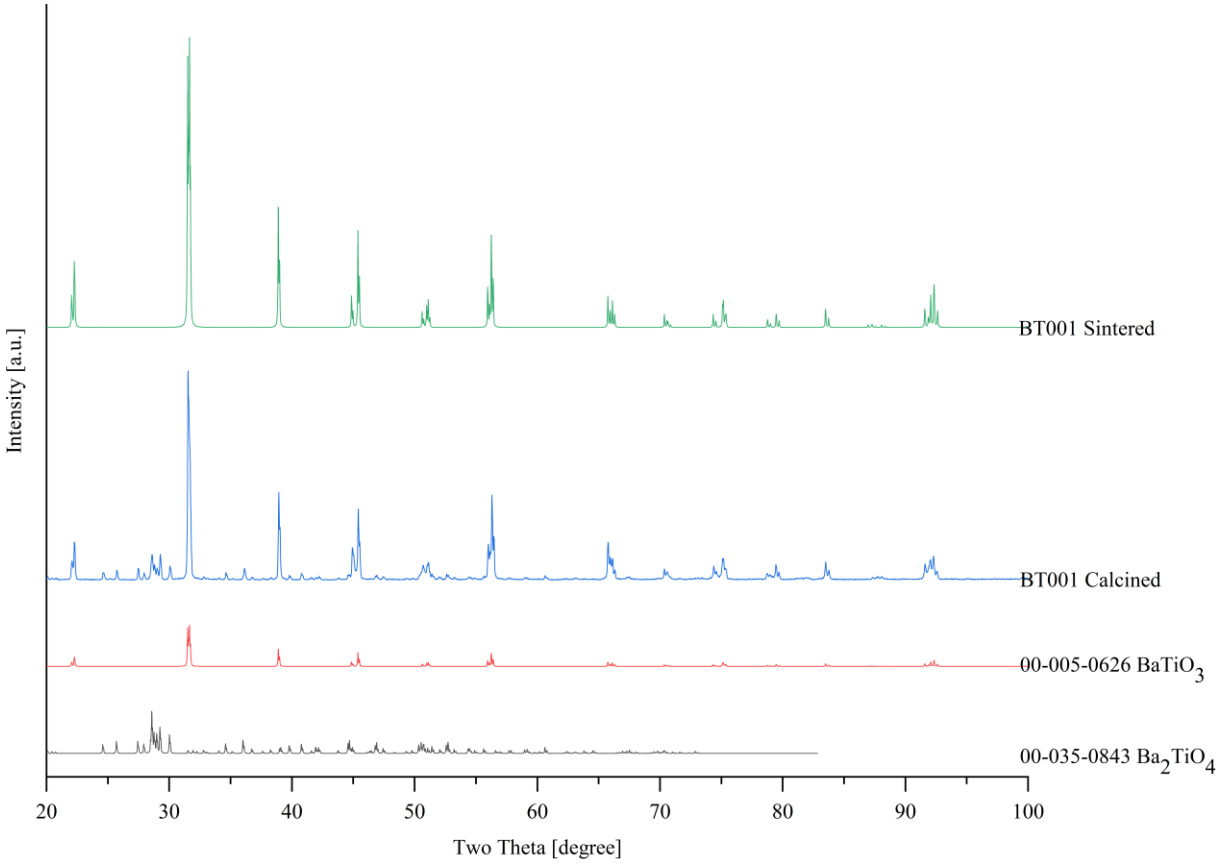


Figure 9 – Sintered BT001, calcined BT001, $BaTiO_3$, and $Ba_2TiO_4$ diffraction patterns.

BT001 is observed as a pure phase perovskite, barium titanate, after the sintering step. Before sintering BT001 is a multiphase material containing both barium orthotitanate ($Ba_2TiO_4$) and barium titanate ($BaTiO_3$). The lattice parameters of BT001 are calculated to be $a$ = 3.9945 Å and $c$ = 4.0345 Å using Reitveld refinement. The lowest substituted material is the only fabricated material that reaches a pure phase upon sintering. Fabricated material compositions BT002, BT003, BT004, BT005, BT006, BT007, and BT008 do not reach pure phases for the described sintering conditions.

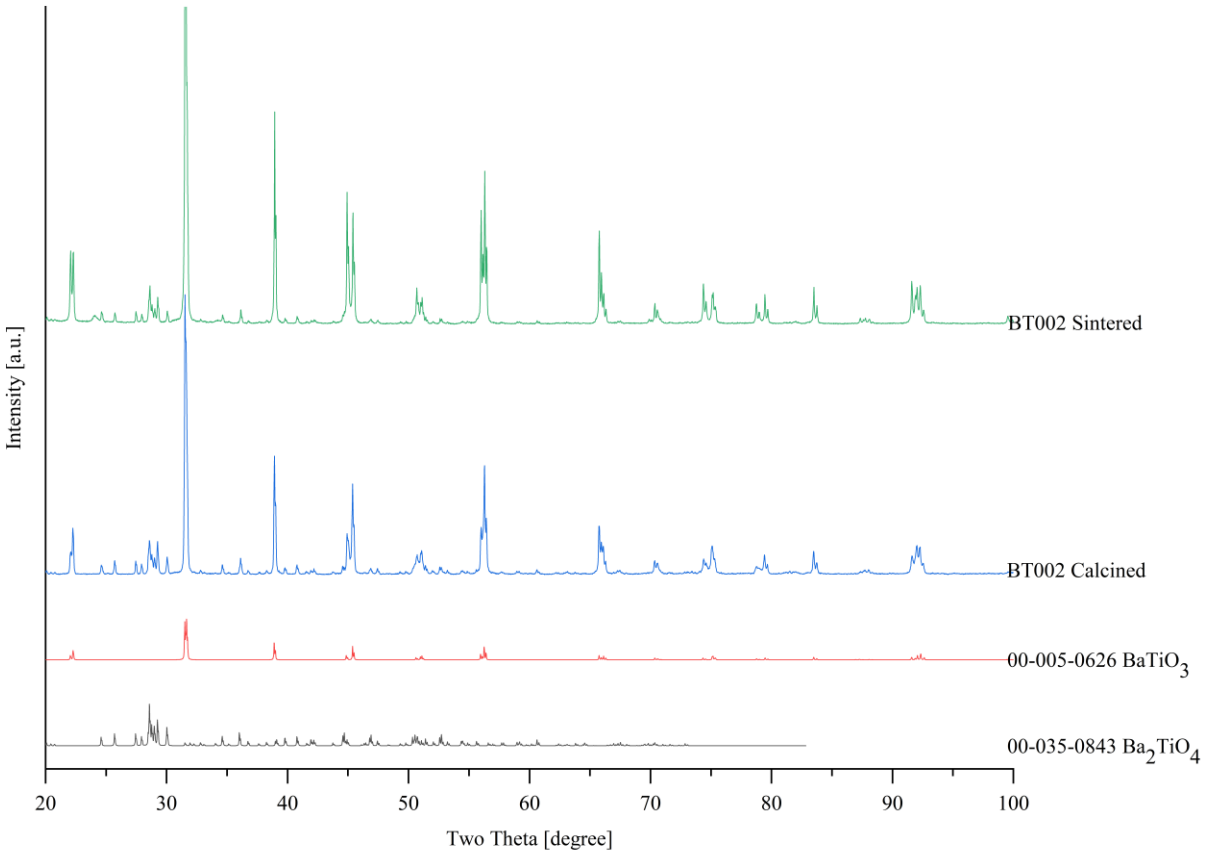


Figure 10 – Sintered BT002, calcined BT002, $BaTiO_3$, and $Ba_2TiO_4$ diffraction patterns.

BT002 does not reach a pure phase perovskite after sintering. There is barium orthotitanate and barium titanate present in the BT002 sintered sample. Using Reitveld refinement at room temperature, the lattice parameters of BT002 are calculated to be $a$ = 3.9947 Å and $c$ = 4.0332 Å.

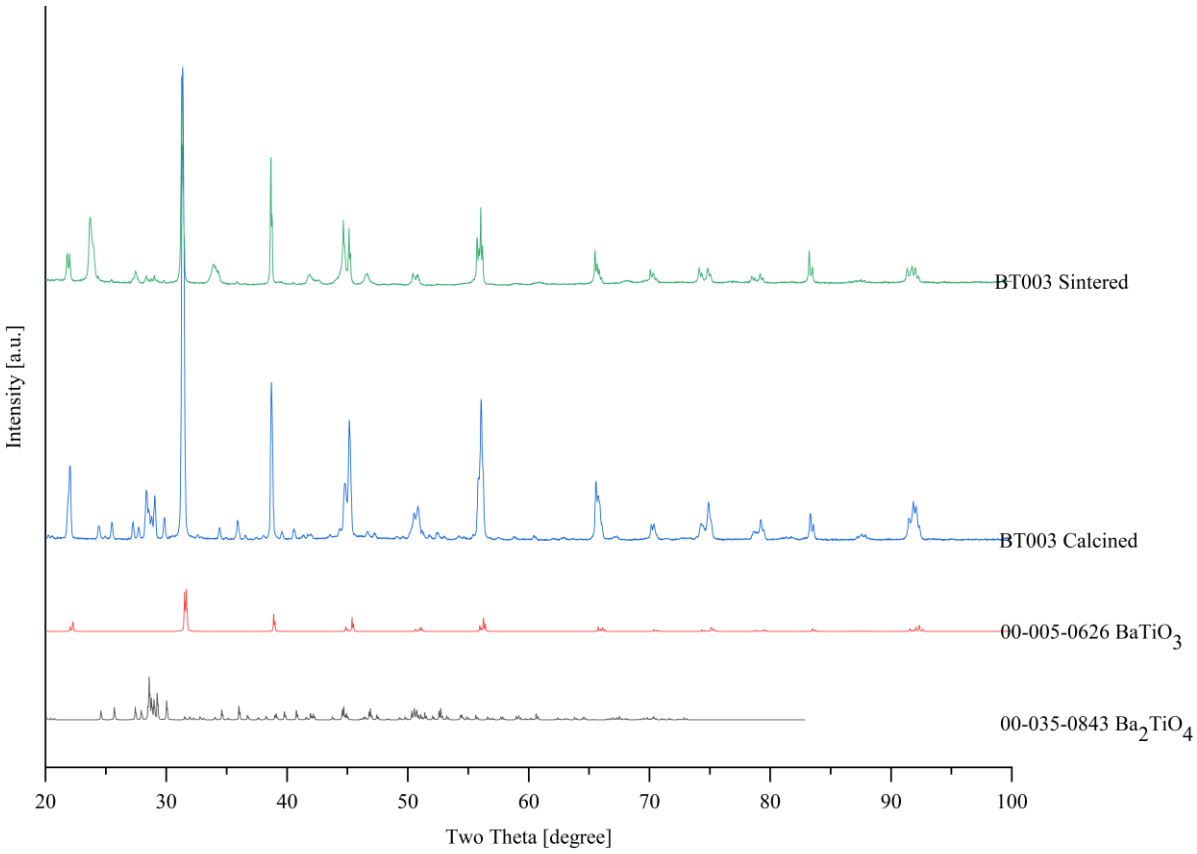


Figure 11 – Sintered BT003, calcined BT003, $BaTiO_3$, and $Ba_2TiO_4$ diffraction patterns.

The lattice parameters of BT003 are calculated to be $a$ = 3.9948 Å and $c$ = 4.0331 Å using Rietveld refinement. For the sintered sample, there is a reflection present at 24° 2θ that is from $Ba_2TiO_4$. The reflection at 24° 2θ is more predominant in BT003 than BT001, BT002, BT004, BT005, BT006, BT007, or BT006.

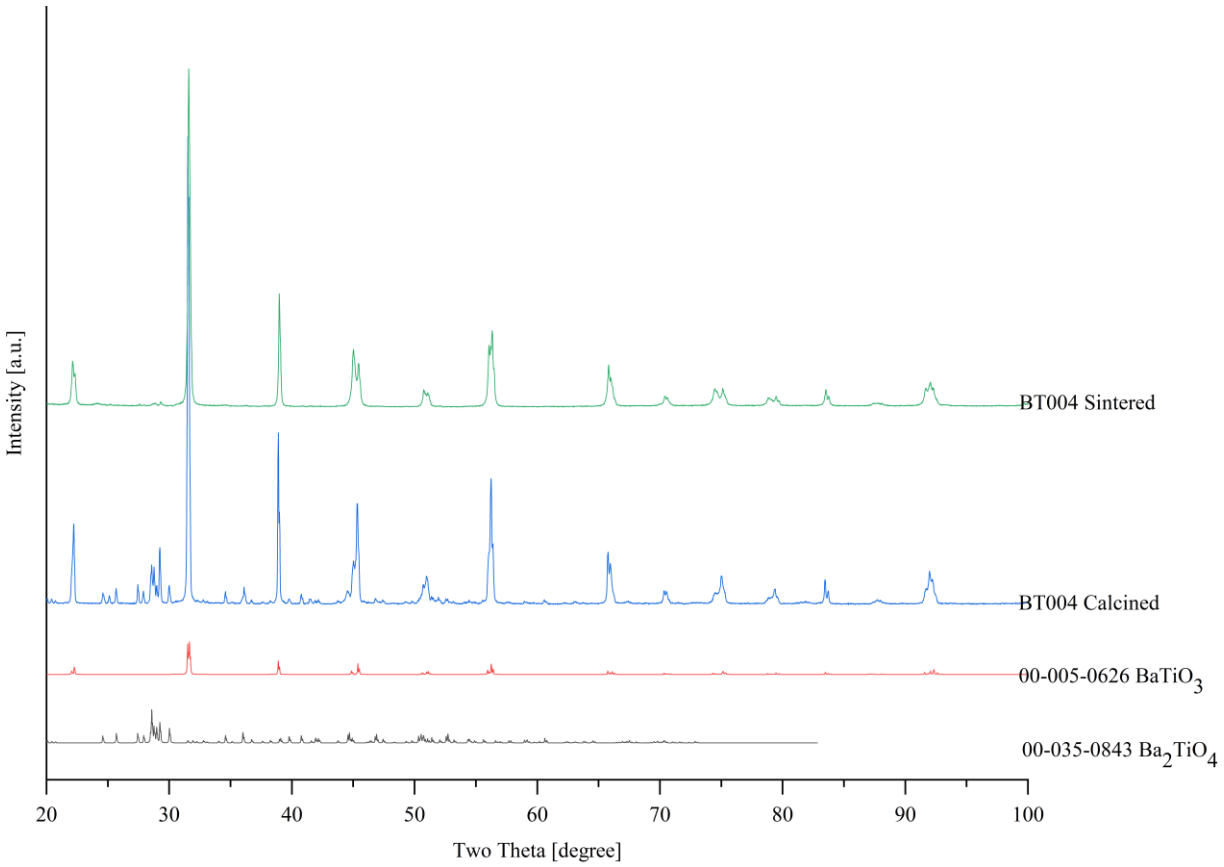


Figure 12 – Sintered BT004, calcined BT004, $BaTiO_3$, and $Ba_2TiO_4$ diffraction patterns.

BT004 is the most phase pure material fabricated containing dipole dopants when compared to BT002, BT003, BT005, BT006, BT007, and BT008. $Ba_2TiO_4$ is present in the sintered BT004, albeit in very small amounts. There are low intensity reflections present at 28° 2θ characteristic of $Ba_2TiO_4$. There is a not a clear reflection shift toward lower 2θ of the prominent peak at 32° 2θ, and therefore the lattice parameter does not drastically change. The lattice parameter of sintered BT004 are calculated to be $a$ = 3.9947 Å and $c$ = 4.0351 Å using Rietveld refinement.

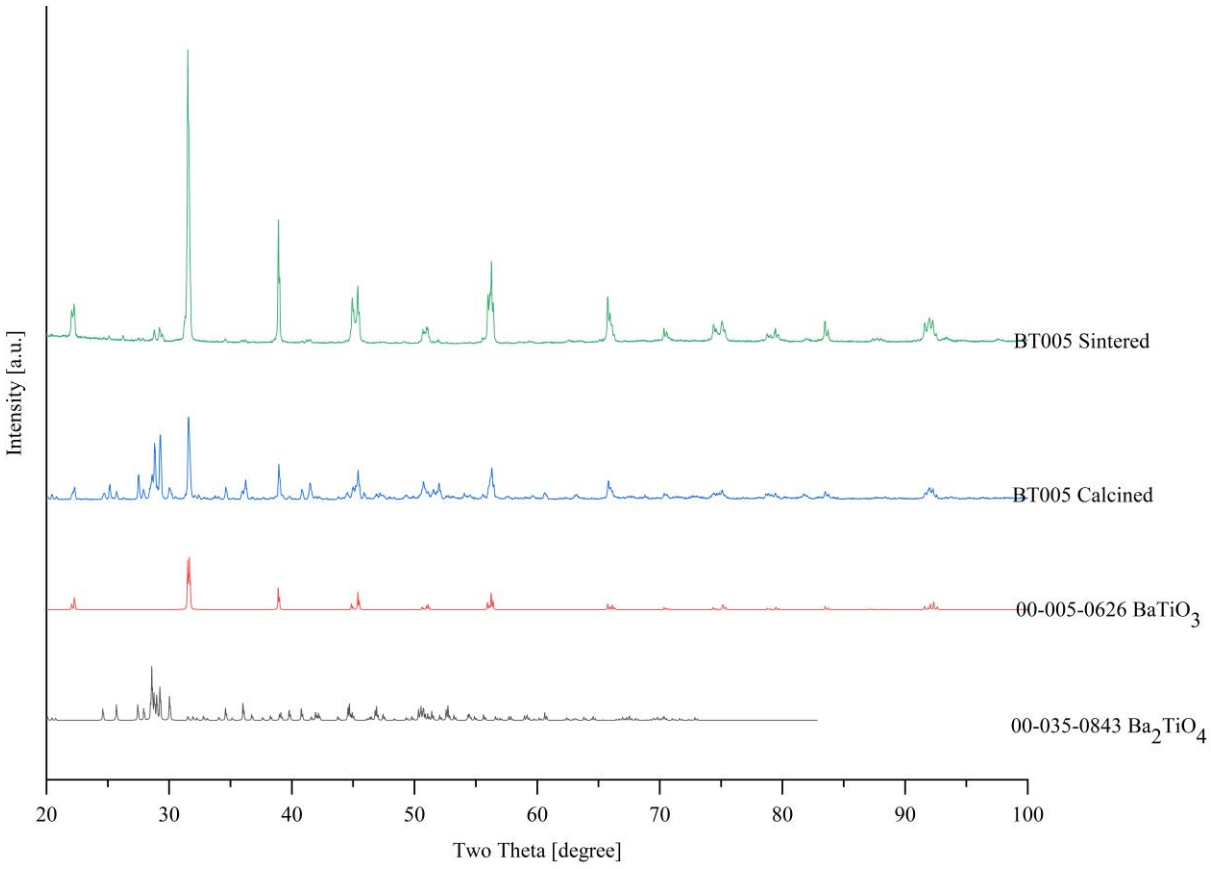


Figure 13 – Sintered BT005, calcined BT005, $BaTiO_3$, and $Ba_2TiO_4$ diffraction patterns.

Sintered BT005 demonstrated an unusual pattern, presenting data resembling a small amorohous hump at diffraction angles lower than 27° 2θ. The sintered BT005 sample was mounted on clay which if exposed to radiation during the measurement may account for the unusual data at low angles. The lattice parameters of sintered BT005 are calculated to be $a$ = 3.9958 Å and $c$ = 4.028 Å using Rietveld refinement.

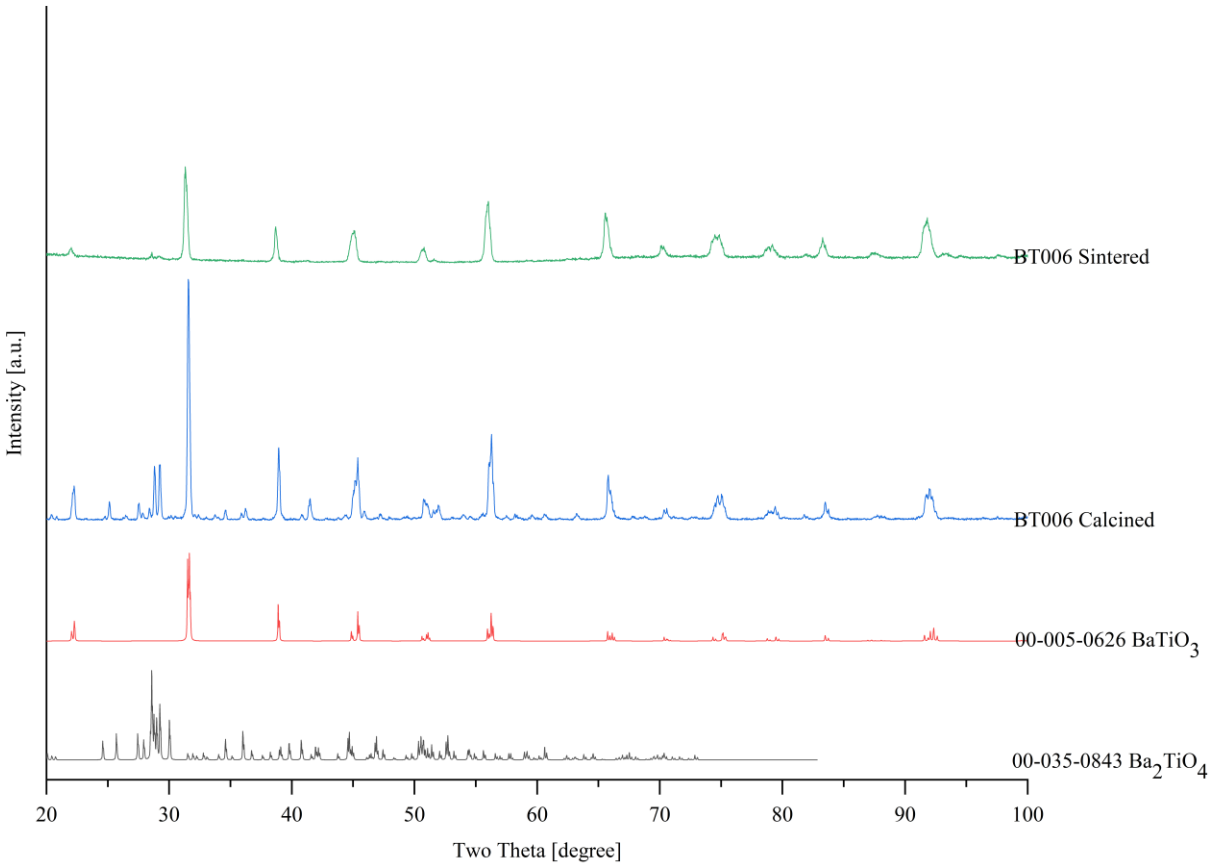


Figure 14 – Sintered BT006, calcined BT006, $BaTiO_3$, and $Ba_2TiO_4$ diffraction patterns.

BT006 does not reach a pure phase perovskite after sintering. There is barium orthotitanate and barium titanate present in the BT006 sintered sample. Using Reitveld refinement at room temperature, the lattice parameters of BT006 are calculated to be $a$ = 3.9969 Å and $c$ = 4.0213 Å.

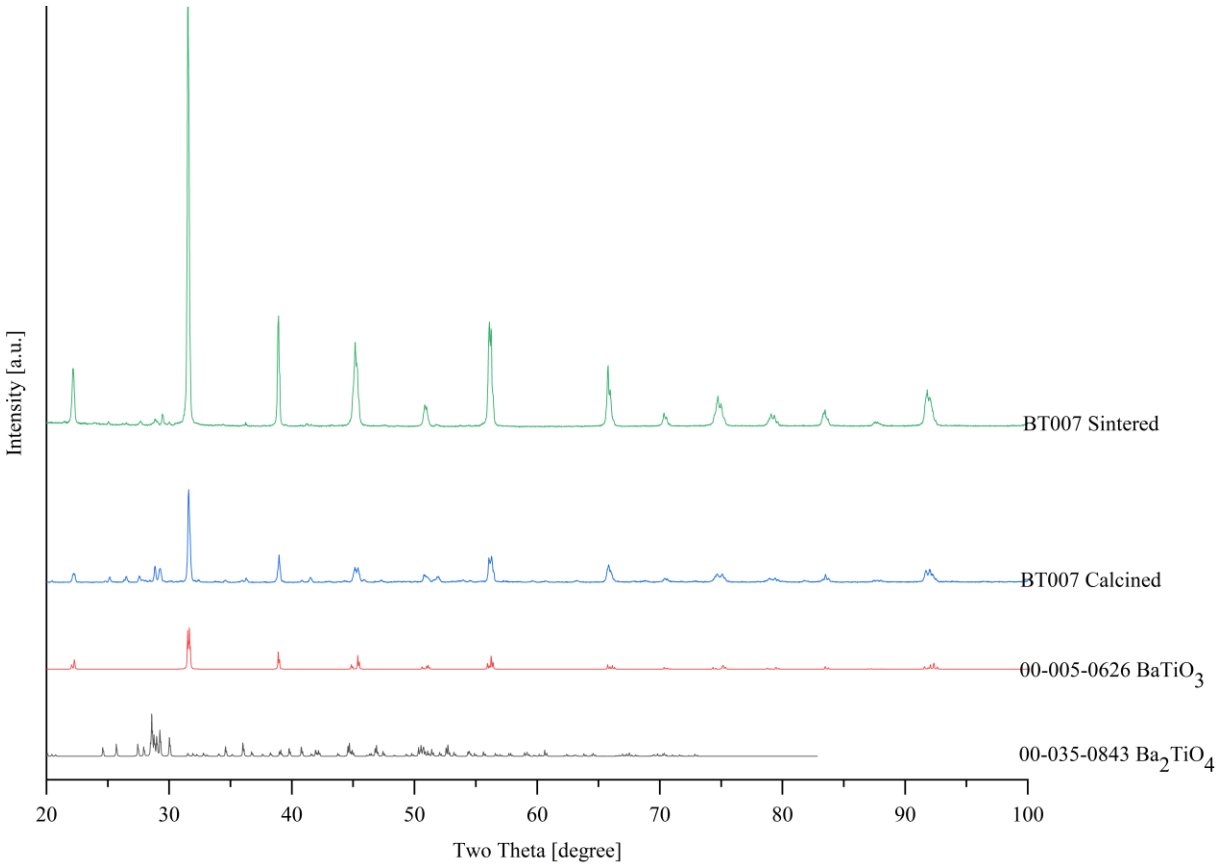


Figure 15 – Sintered BT007, calcined BT007, $BaTiO_3$, and $Ba_2TiO_4$ diffraction patterns.

BT007 does not reach a pure phase perovskite after sintering. There is barium orthotitanate and barium titanate present in the BT007 sintered sample. Using Reitveld refinement at room temperature, the lattice parameters of BT007 are calculated to be $a$ = 3.9970 Å and $c$ = 4.0119 Å.

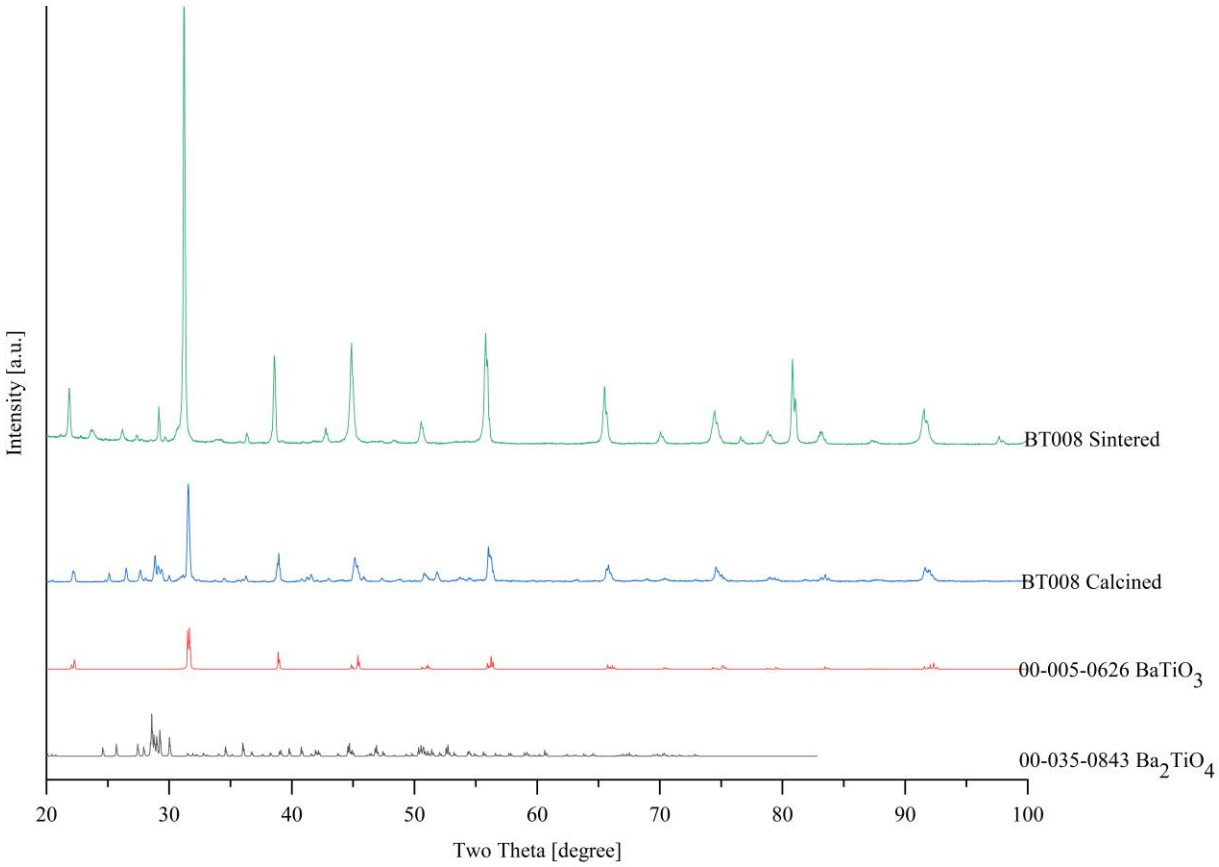


Figure 16 – Sintered BT008, calcined BT008, $BaTiO_3$, and $Ba_2TiO_4$ diffraction patterns.

BT008 does not reach a pure phase perovskite after sintering. There is barium orthotitanate and barium titanate present in the BT008 sintered sample. Using Reitveld refinement at room temperature, the lattice parameters of BT008 are calculated to be $a$ = 4.0013 Å and $c$ = 4.0010 Å.

Lattice parameters *a* and *c* of samples BT001, BT002, BT003, BT004, BT005, BT006, BT007, and BT008 are summarized in Table VIII. Systematic error from diffraction instrumentation is not fully accounted for in lattice parameter calculations.

Table VIII – Calculated lattice parameters of fabricated materials, error = ±0.0001 Å.

| **Sample Name** | **Lattice Parameter *a* [Å]** | **Lattice Parameter *c* [Å]** | $\frac{c}{a}$ |
|---|---|---|---|
| BT001 | 3.9945 | 4.0345 | 1.0100 |
| BT002 | 3.9947 | 4.0332 | 1.0096 |
| BT003 | 3.9948 | 4.0331 | 1.0096 |
| BT004 | 3.9947 | 4.0351 | 1.0101 |
| BT005 | 3.9958 | 4.0288 | 1.0083 |
| BT006 | 3.9969 | 4.0213 | 1.0061 |
| BT007 | 3.9970 | 4.0119 | 1.0037 |
| BT008 | 4.0013 | 4.0010 | 0.9999 |

As dopant concentration increases, the lattice parameter *a* increases as the lattice parameter *c* decreases. The data supports the hypothesis that dipoles are being incorporated with the formed lattice, causing a solid solution matrix. According the Shannon's revised ionic radii model, $Cu^{2+}$ and $W^{6+}$ have effective ionic radii of 73 pm and 60.5 pm, respectively [16]. $Ti^{4+}$ has a reported ionic radius of 60 pm [16]. A dipole created with $Cu^{2+}$ and $W^{6+}$ at each pole gives a charge average of 4+, and therefore is conducive to substituting into the B site of the lattice where $Ti^{4+}$ typically is located in $BaTiO_3$. Furthermore, the relatively similar effective ionic radii of each ion considered ($Cu^{2+}$, $W^{6+}$, $Ti^{4+}$) facilitates the substitution of $Cu^{2+}$ and $W^{6+}$ into the B site to form dipoles. If it were the case that $Cu^{2+}$ and $W^{6+}$ were not substituting into the lattice, their would-be indications of such in diffraction experiments.

There are no such indications, and instead there are clear indications of a solid solution forming. Figure 16 gives the c/a ratio as a function of dopant concentration.

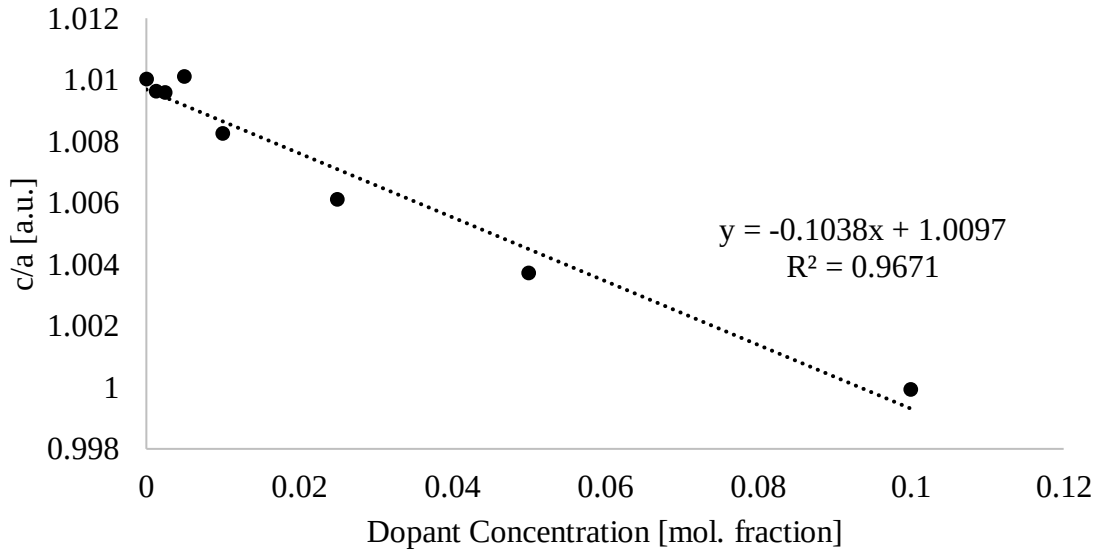


Figure 17 – The c/a ratio as a function of dopant concentration. An inversely proportional trend is observed.

The c/a ratio of the Cu – W dipole pair materials decreases at a slower rate than the Ga – Ta dipole pair materials studied by Veerapandiyan. Furthermore, the resistivity values of the Cu – W dipole pair materials is significantly improved over Ga – Ta dipole pair materials. The Cu – W dipole is a stronger dipole because of a larger charge disparity than the Ga – Ta dipole, and therefore is likely responsible for the observed increase in resistivity. Barium orthotitanate ($Ba_2TiO_4$) is phase cited [6] as an intermediate in the solid-state reaction pathway to forming $BaTiO_3$, and therefore it is not alarming that it is present in most of the fabricated materials. The presence of $Ba_2TiO_4$ indicates that the sintering step must occur for longer times than 24 hours and/or at a higher temperature than 1350 °C.

C. ELECTRICAL RESISTIVITY

The electrical resistivity of BT001, BT002, BT003, BT004, BT005, BT006, BT007, and BT008 have been measured over the temperature range [20, 500] °C. As dipole concentration increases, the resistivity of the material is shown to systematically increase. Additionally, the dependence of each materials resistivity on temperature increased with dopant concentration. Figure 17 provides the resistivity of each fabricated material as a function of temperature.

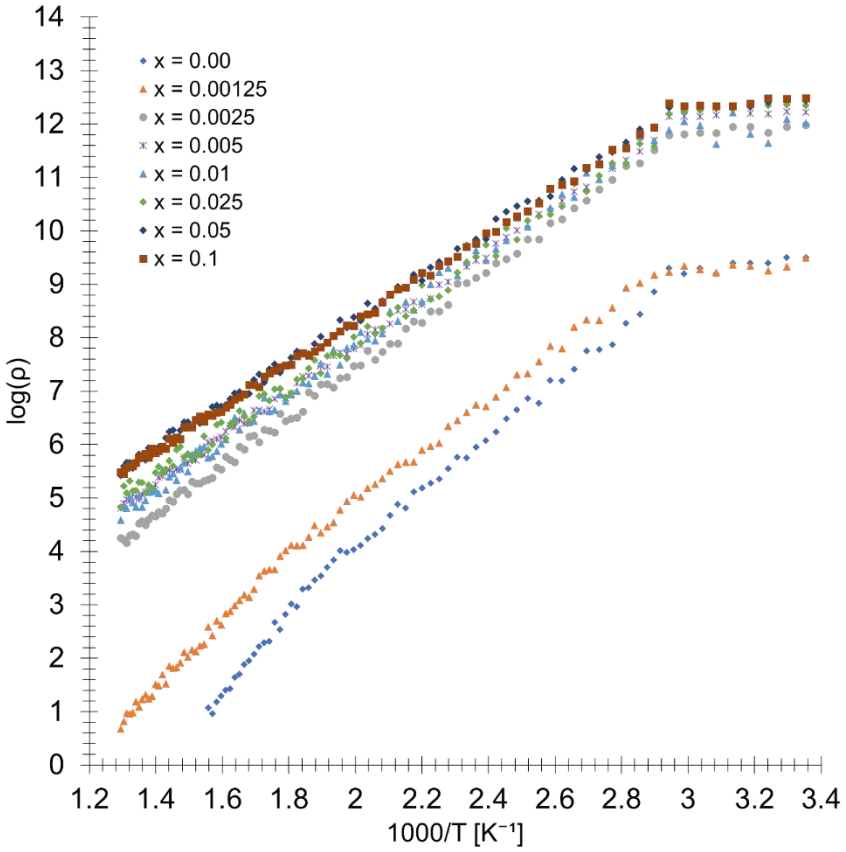


Figure 18 – Temperature dependent electrical resistivity measurement. Break in linear trends indicates phase transition. Calculated activation energies are located in Table IX.

The paraelectric region of each material is observed in the linear regions of Figure 16. Changes in slope are observed around 555 K and 357 K in BT001 and BT002, respectively. The changes in slope are indicative of phase transitions. The phase transitions at 555 K is not observed in BT003, BT004, BT005, BT006, BT007, or BT008. However, the phase transition at around 357 K is observed in BT003, BT004, BT005, BT006, BT007, or BT008. These phase transitions are shifted systematically to lower temperature as dopant concentration increases, thereby possibly indicating a broadening of the paraelectric region as dopant concentration increases. Activation energies are calculated from the slope of the paraelectric region of each material and are given in Table IX.

Table IX – Activations energies of fabricated materials.

| **Sample Name** | **Activation Energy [eV]** |
|---|---|
| BT001 | 0.42 |
| BT002 | 0.41 |
| BT003 | 0.40 |
| BT004 | 0.37 |
| BT005 | 0.38 |
| BT006 | 0.36 |
| BT007 | 0.35 |
| BT008 | 0.35 |

The activation energy of each material is indicative of the materials sensitivity to temperature change. The higher the activation energy, the more sensitive the parameter of the material is to temperature change. The activation energy and resistivity of the material increases systematically with dipole dopant concentration, except for the case of BT005.

When compared to BT004 activation energy 0.37 eV, BT005 has a higher activation energy of 0.38 eV. The resistivity of materials BT003, BT004, BT005, BT006, BT007, or BT008 are greatly improved over materials BT001 and BT002. A comparison of resistivity at RT is given in Table X.

Table X – RT electrical resistivity of fabricated materials.

| **Sample Name** | **Resistivity at RT [Ωm]** |
|---|---|
| BT001 | $\sim 10^{9}$ |
| BT002 | $\sim 10^{9}$ |
| BT003 | $\sim 10^{12}$ |
| BT004 | $\sim 10^{12}$ |
| BT005 | $\sim 10^{12}$ |
| BT006 | $\sim 10^{12}$ |
| BT007 | $\sim 10^{12}$ |
| BT008 | $\sim 10^{12}$ |

# CONCLUSIONS AND FUTURE WORK

The electrical properties of fabricated materials improved, made evident by the increase in electrical resistivity values observed as a function of increasing dipole substitution concentration. Future work should include the following material fabrication improvements: increased time and temperature sintering steps to increase density of materials. With increase time and temperature of sintering, the density is hypothesized to increase as well as the incidence of phase pure materials. In-situ high temperate X-ray diffraction should be conducted to explore structural hypotheses as dependent on dipole concentration. Further electrical measurements should be taken to evaluate the permittivity and break down strength characteristics of fabricated materials.

# LITERATURE REFERENCES


1. V. Veerapandiyan, "Inducing Diffuse Phase Transitions in Barium Titanate Using Ga3+-Ta5+ Dipole Pair Substituents"; Master of Science Thesis. Alfred University, New York State College of Ceramics, 2017.

2. X. K. Letao Yang, Fei Li, Hua Hao, Zhenxiang Cheng, Hanxing Liu, Jing-Feng Li, Shujun Zhang, "Perovskite Lead-Free Dielectrics for Energy Storage Applications," *pmatsci,* **102** 72-108 (2019).

3. J. B. Daniel Akinyele, Yoash Levron, "Battery Storage Technologies for Electrical Applications: Impact in Stand-Alone Photovoltaic Systems," *Energies,* **10** [11] (2017).

4. K. T. Nandini Jaiswal, Rathod Suman, Devendra Kumar, Shail Upadhyay, Om Parkash, "A Brief Review on Ceria Based Solid Electrolytes for Solid Oxide Fuel Cells," *Journal of Alloys and Compounds,* **781** 984-1005 (2019).

5. P. P. L. Fulay, J. K., *Electronic, Magnetic, and Optical Materials*. CRC Press, Boca Raton, FL, 2017.

6. C. H. Pithan, D.; Waser, R., "Progress in the Synthesis of Nanocrystalline Batio3 Powders for Mlcc," *International Journal of Applied Ceramic Technology,* **2** [1] 1 - 14 (2005).

7. G. S. ROHRER, "Structure and Bonding in Crystalline Materials"; pp. 135-202 in. Cambridge University Press, Crystal Structures, 2001.

8. J. William D. Callister, David G. Rethwisch, "Fundamentals of Materials Science and Engineering: An Integrated Approach"; pp. 483-541 in. John Wiley & Sons, Electrical Properties, 2012.

9. H. A. GATEA, "Impact of Sintering Temperature on Structural and Dielectric Properties of Barium Strontium Titanate Prepared by Sol-Gel Metho," *Journal of Ovanic Research,* **14** [6] 467-74 (2018).

10. J.-K. L. Pradeep Fuley, in ŦElectronic, Magnetic, and Optical Materialsƴ (Y. Gogotsi, ed.), p. 329-402. CNC Press, 2017.

11. S. C. Tidrow, 2019, Private Communication.

12. C. Learner, "Barium Titanate" Chemistry Learner. Accessed on: 2019. Available at <http://www.chemistrylearner.com/barium-titanate.html>

13. A. Materials, "Barium Titanate ($Batio_3$) - Properties and Applications" (2004) AZoM. Accessed on: 2019. Available at <https://www.azom.com/article.aspx?ArticleID=2280>

14. F. Scientific, "Material Safety Data Sheet Barium Titanate(Iv), 99%" Fischer Scientific. Accessed on: Available at <https://fscimage.fishersci.com/msds/58263.htm>

15. SIGMA-ALDRICH, "Barium Titanate (Iv)" SIGMA-ALDRICH. Accessed on: 2019. Available at <https://www.sigmaaldrich.com/catalog/product/aldrich/208108?lang=en&region=US>

16. R. D. Shannon, "Revised Effective Ionic Radii and Systematic Studies of Interatomie Distances in Halides and Chaleogenides " *Acta. Cryst.,* **32** (1976).